Progress In Electromagnetics Research M, Vol. 111, 1–12, 2022

Generalized Design Methodology of Highly Efficient Quad-Furcated Profiled Horns with Larger Apertures

Charalampos Stoumpos[1, *], Jean-Philippe Fraysse[2], George Goussetis[3], Ronan Sauleau[1], and Hervé Legay[2]

Abstract—In this work we demonstrate the extended and generalized methodology for the design of Quad-Furcated Profiled Horns (Q-FPHs). Based on a design case of a $4\lambda_0 \times 4\lambda_0$ Q-FPH, we extract the Generalized Scattering Matrix (GSM) of the enlarged quad-furcated discontinuity and provide analytical expressions for its multimode feeding. Next, the four feeding and the upper common waveguide sections are optimized accordingly through Mode-Matching (MM). The high aperture efficiency levels delivered by the methodology are verified by full-wave simulations of the optimized design case and compared to the state-of-the-art which is thereby redefined.

1. INTRODUCTION

Horn antenna is the most common radiator in satellite applications deployed as feed elements for reflectors or in phased arrays, owing to its favourable electrical performance [1]. Over more than two decades, industry relies on the profiled horns, being those radiators that can achieve the best aperture efficiency × bandwidth product [2–5]. The concept of hard [6] and metamaterial-based horns [7] has been proved to be an appealing high aperture efficiency candidate as well; however, materials properties and electrostatic discharge (ESD) effects pose significant obstacles at spaceborne applications.

The concept of utilizing more than one multimode waveguide access to feed the radiating aperture of a horn was recently developed [8, 9]. Highly efficient, compact, and broadband horns were designed and manufactured in single [10] and dual polarizations [11], redefining the state-of-the-art. Both of these multi-access radiators present aperture sizes from $2.6\lambda_0$ to $2.8\lambda_0$; typical aperture sizes for Geostationary Orbit (GEO) antennas.

This work comes to generalize and complement the design methodology of highly efficient Q-FPHs with apertures larger than the typical GEO application-based aperture regime [12]. The necessity for realizing horn antennas with larger aperture sizes is driven by two parameters. The first one relates to the sparse arrays, which are configurations that employ different antenna apertures and are used for the mitigation of grating lobes [13]. The second parameter relates to dual-band applications [1, 2, 14], where typically one horn antenna followed by a dual-band OMT and a diplexer covers both Tx and Rx bands. For a large frequency separation between the two bands, the electric size of the antenna aperture gets values around $4\lambda_0$ for the latter band.

We present, here, analytical expressions and explicit design rules based on the design case of a $4\lambda_0 \times 4\lambda_0$ aperture Q-FPH. The numerically computed results are verified by full-wave simulations demonstrating the extensibility and robustness of the design methodology for the conception of such elements.

Received 11 April 2022, Accepted 19 May 2022, Scheduled 3 June 2022

* Corresponding author: Charalampos Stoumpos (Charalampos.Stoumpos@insa-rennes.fr, haris_stou@hotmail.com).

[1] Univ. Rennes, CNRS, Institut d'Electronique et des Technologies du numéRique (IETR) — UMR CNRS 6164, F-35000 Rennes, France. [2] Research and Development Department, Thales Alenia Space, Toulouse 31037, France. [3] School of Engineering and Physical Sciences, Heriot-Watt University, EH14 4AS, Edinburgh, UK.

2. DESIGN PRINCIPLES

There are two principal differences for design cases of Q-FPHs with larger apertures. The first is that a greater number of aperture modes is involved, while the second relates to the potential of generating more excitation modes in the form of TE_{m0}, $m = 1, 2, 3, ...$, at the four feeding waveguide parts. The first factor suggests that the theoretical maximum aperture efficiency bounds are enlarged up to 95.1% [3, 15]. This also adds complexity in the design since more modes should be considered at the calculations. However, the proposed methodology relies principally on the design of the feeding waveguide sections. These present a physically smaller (half at most) output section than the final radiating aperture. This is translated into fast optimization of its structure especially when MM is used.

The analysis commences with the calculation of the 4-furcation's GSM. After interpreting its modal couplings, we create a system of equations upon which the excitation modes will be defined. Then, only one excitation waveguide section is designed accordingly so that being when connected to the 4-furcation, its common port can excite the desired set of propagating and radiating modes TE_{m0}, $m = 1, 3, 5, 7$. As a final step, the finite length of this common waveguide section will align the phase of the radiating modes. Fig. 1 shows the optimized geometry of the four-port $4\lambda_0 \times 4\lambda_0$ horn designed according to the

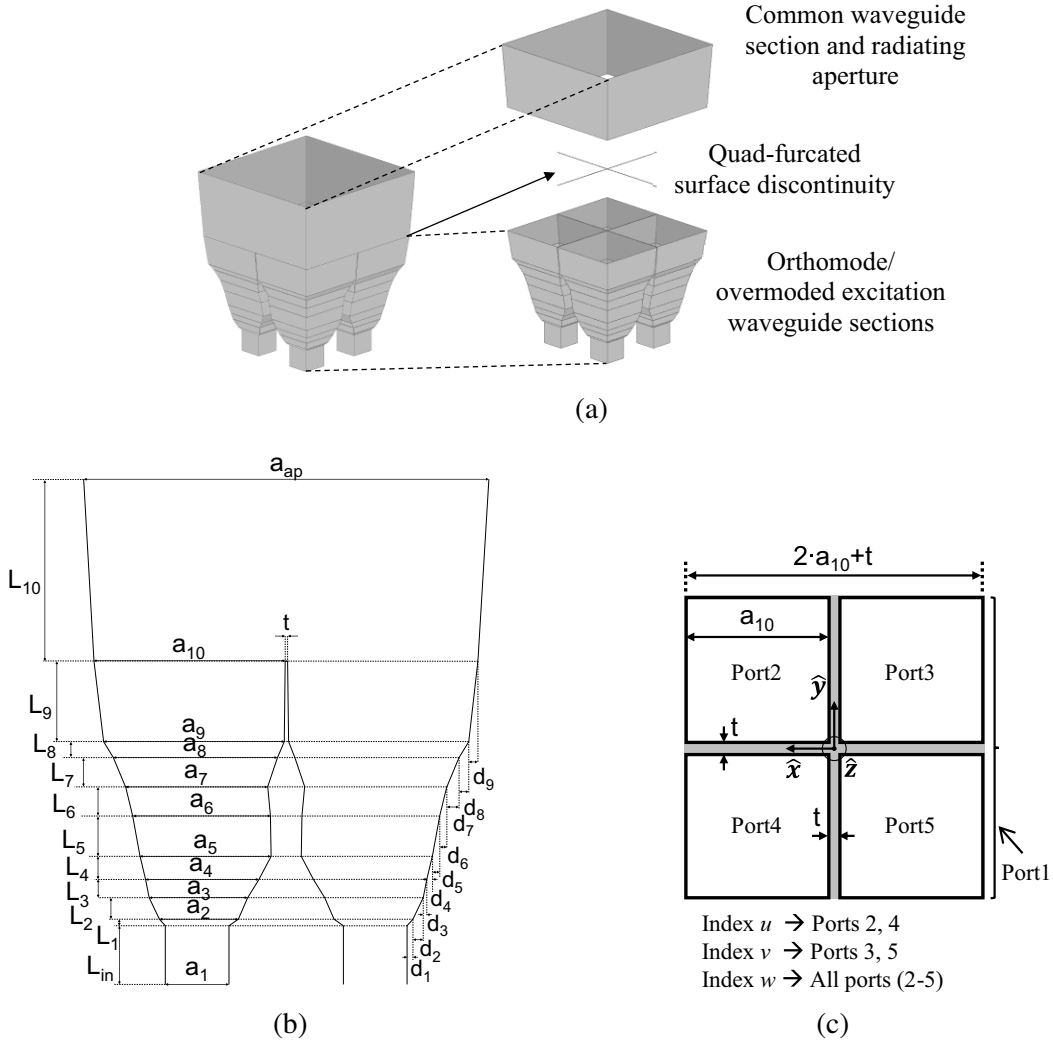

Figure 1. Geometry and layout of the quad-furcated profiled horn with a $4\lambda_0 \times 4\lambda_0$ square aperture: (a) perspective and exploded view, (b) side cut-view with dimensional variables and (c) definition and geometry of the quad-furcated surface waveguide discontinuity.

presented methodology. From Fig. 1(b), the optimized geometrical parameters are as follows.

1. $a_i = \{16.05, 19.9, 25.07, 28.66, 33.154, 34.78, 35.97, 41.43, 45.513, 48.25\}$ mm.
2. $d_i = \{1.575, 2.625, 0.805, 1.437, 1.837, 1.905, 2.943, 2.5215, 2.3385\}$ mm.
3. $L_i = \{1.68, 5.73, 4.12, 6.06, 10.12, 7.42, 7.33, 3.98, 20.26, 45.762\}$ mm.
4. $\{L_{in}, t, a_{ap}\} = \{15, 0.4, 102.27461253731\}$ mm.

2.1. Modal Analysis and Results of the Quad-Furcated Surface Waveguide Discontinuity

The transmission coefficients of the quad-furcated surface waveguide discontinuity's GSM among the excitation modes are plotted in amplitude and phase in Figs. 2(a)–(c) and 3(a)–(d), respectively. These are used to formulate the coupling matrix of the quad-furcation. The appropriate aperture modal vector for maximum directivity will be then assigned as solution to the final system of equations. From this system, the excitation modes will be defined. The indices w, u, and v of the 4-furcation's waveguide accesses are mentioned in Fig. 1(c).

The non-normalized output modal vector expressed as a function of the 4-furcation's transmission

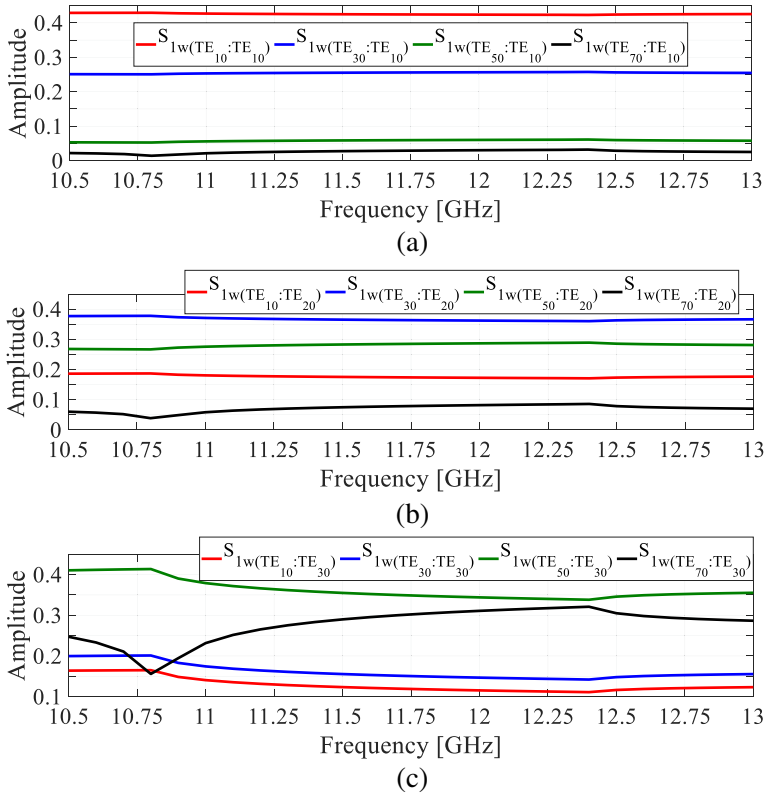

Figure 2. Amplitude of the modal transmission coefficients among the modes TE_{m0}, $m = 1, 2, 3$ of the four ($w = 2, 3, 4, 5$) feeding waveguides and the modes TE_{m0}, $m = 1, 3, 5, 7$ of the common waveguide for the 4-furcated surface discontinuity: (a) among the feeding modes TE_{m0} and the common waveguide mode TE_{10}, (b) among the feeding modes TE_{m0} and the common waveguide mode TE_{20} and (c) among the feeding modes TE_{m0} and the common waveguide mode TE_{30}.

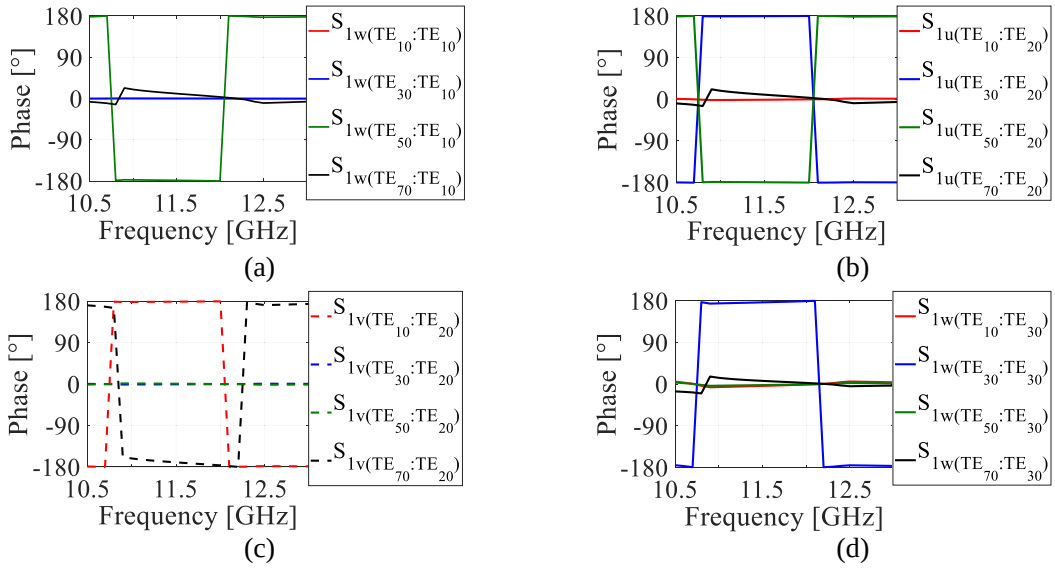

Figure 3. Phase of the modal transmission coefficients among the modes TE_{m0}, $m = 1, 2, 3$ of the four ($w = 2, 3, 4, 5$) feeding waveguides and the modes TE_{m0}, $m = 1, 3, 5, 7$ of the common waveguide for the 4-furcated surface discontinuity: (a) among the feeding modes TE_{m0} and the common waveguide mode TE_{10}, (b) among the feeding modes TE_{m0} and the common waveguide mode TE_{20} and (c) among the feeding modes TE_{m0} and the common waveguide mode TE_{30}.

coefficients and the feeding modal amplitudes can be now written as follows:

$$\begin{bmatrix} F_1^{h_{10}} \\ F_1^{h_{30}} \\ F_1^{h_{50}} \\ F_1^{h_{70}} \end{bmatrix} = \frac{1}{2} \begin{bmatrix} \sum_{w=2}^{5} \left(F_w^{h_{10}} \cdot S_{1w(h_{10}:h_{10})} + F_w^{h_{20}} \cdot S_{1w(h_{10}:h_{20})} + F_w^{h_{30}} \cdot S_{1w(h_{10}:h_{30})} \right) \\ \sum_{w=2}^{5} \left(F_w^{h_{10}} \cdot S_{1w(h_{30}:h_{10})} + F_w^{h_{20}} \cdot S_{1w(h_{30}:h_{20})} + F_w^{h_{30}} \cdot S_{1w(h_{30}:h_{30})} \right) \\ \sum_{w=2}^{5} \left(F_w^{h_{10}} \cdot S_{1w(h_{50}:h_{10})} + F_w^{h_{20}} \cdot S_{1w(h_{50}:h_{20})} + F_w^{h_{30}} \cdot S_{1w(h_{50}:h_{30})} \right) \\ \sum_{w=2}^{5} \left(F_w^{h_{10}} \cdot S_{1w(h_{70}:h_{10})} + F_w^{h_{20}} \cdot S_{1w(h_{70}:h_{20})} + F_w^{h_{30}} \cdot S_{1w(h_{70}:h_{30})} \right) \end{bmatrix} \tag{1}$$

From Figs. 3(a)–(d) and assuming $\hat{y}$ as the reference polarization axis, the following phase conditions are derived:

$$\left| \varphi_{S^c_{1u,h_{m0}\to h_{m'0}}} - \varphi_{S^c_{1v,h_{m0}\to h_{m'0}}} \right| = 0^\circ \Rightarrow e^{j\varphi_{S^c_{1u,h_{m0}\to h_{m'0}}}} = e^{j\varphi_{S^c_{1v,h_{m0}\to h_{m'0}}}},$$
$$u = 2, 4,\ v = 3, 5,\ m = 1, 3, 5, 7\,\&\,m' = 1, 7 \tag{2a}$$

$$\left| \varphi_{S^c_{1w,h_{50}\to h_{10}}} - \varphi_{S^c_{1w,h_{m''0}\to h_{10}}} \right| = 180^\circ \Rightarrow e^{j\varphi_{S^c_{1w,h_{50}\to h_{10}}}} = -e^{j\varphi_{S^c_{1w,h_{m''0}\to h_{10}}}},$$
$$w = 1, 2, 3, 4\,\&\,m'' = 1, 3, 7 \tag{2b}$$

$$\left| \varphi_{S^c_{1w,h_{50}\to h_{30}}} - \varphi_{S^c_{1w,h_{m''0}\to h_{30}}} \right| = 0^\circ \Rightarrow e^{j\varphi_{S^c_{1w,h_{50}\to h_{30}}}} = e^{j\varphi_{S^c_{1w,h_{m''0}\to h_{30}}}},$$
$$w = 1, 2, 3, 4\,\&\,m'' = 1, 3, 7 \tag{2c}$$

$$\left| \varphi_{S^c_{1u,h_{m0}\to h_{20}}} - \varphi_{S^c_{1v,h_{m0}\to h_{20}}} \right| = 180^\circ \Rightarrow e^{j\varphi_{S^c_{1u,h_{m0}\to h_{20}}}} = -e^{j\varphi_{S^c_{1v,h_{m0}\to h_{20}}}},$$
$$u = 2, 4,\ v = 3, 5\,\&\,m = 1, 3, 5, 7 \tag{2d}$$

$$\left|\varphi_{S^c_{1u,h_{30}\to h_{10}}} - \varphi_{S^c_{1u,h_{30}\to h_{m'''0}}}\right| = 180^\circ \Rightarrow e^{j\varphi_{S^c_{1u,h_{30}\to h_{10}}}} = -e^{j\varphi_{S^c_{1u,h_{30}\to h_{m'''0}}}}, \quad \text{where } u = 2,4 \,\&\, m''' = 2,3 \tag{2e}$$

$$\left|\varphi_{S^c_{1v,h_{30}\to h_{10}}} - \varphi_{S^c_{1v,h_{30}\to h_{m'''0}}}\right| = 0^\circ \Rightarrow e^{j\varphi_{S^c_{1v,h_{30}\to h_{10}}}} = e^{j\varphi_{S^c_{1v,h_{30}\to h_{m'''0}}}}, \quad \text{where } v = 3,5 \,\&\, m''' = 2,3 \tag{2f}$$

$$\left|\varphi_{S^c_{1u,h_{70}\to h_{30}}} - \varphi_{S^c_{1v,h_{70}\to h_{30}}}\right| = 0^\circ \Rightarrow e^{j\varphi_{S^c_{1u,h_{70}\to h_{30}}}} = e^{j\varphi_{S^c_{1v,h_{70}\to h_{30}}}}, \quad u = 2,4 \,\&\, v = 3,5 \tag{2g}$$

If $|h^{in}_{20}| \neq 0$, $|S^c_{1w,h_{m0}\to h_{20}}| \neq 0$, $m = 1, 3, 5$, each second term of every summation in Eq. (1) will be suppressed, and there will no longer be a contribution from the mode TE_{20}, if and only if $\varphi_{w,h_{20}}$ is the same $\forall w = 2, 3, 4, 5$ due to Eq. (2d). Thus, the excitation waveguides should be designed so as to comply with the following relation:

$$\left|\varphi_{u,h^{in}_{20}} - \varphi_{v,h^{in}_{20}}\right| = 180^\circ \Rightarrow e^{j\varphi_{u,h^{in}_{20}}} = -e^{j\varphi_{v,h^{in}_{20}}}, \quad u = 2,4 \,\&\, v = 3,5 \tag{3}$$

After including Eqs. 2(a)–(g) and (3) into (1), occurs:

$$\begin{bmatrix} F_1^{h_{10}} \\ F_1^{h_{30}} \\ F_1^{h_{50}} \\ F_1^{h_{70}} \end{bmatrix}$$

$$= 2\begin{bmatrix} |h^{in}_{10}| \cdot e^{j\varphi_{2,h^{in}_{10}}} \cdot \left|S^c_{12,h_{10}\to h_{10}}\right| + |h^{in}_{20}| \cdot e^{j\varphi_{2,h^{in}_{20}}} \cdot \left|S^c_{12,h_{10}\to h_{20}}\right| + |h^{in}_{30}| \cdot e^{j\varphi_{2,h^{in}_{30}}} \cdot \left|S^c_{12,h_{10}\to h_{30}}\right| \\ |h^{in}_{10}| \cdot e^{j\varphi_{2,h^{in}_{10}}} \cdot \left|S^c_{12,h_{30}\to h_{10}}\right| - |h^{in}_{20}| \cdot e^{j\varphi_{2,h^{in}_{20}}} \cdot \left|S^c_{12,h_{30}\to h_{20}}\right| - |h^{in}_{30}| \cdot e^{j\varphi_{2,h^{in}_{30}}} \cdot \left|S^c_{12,h_{30}\to h_{30}}\right| \\ -|h^{in}_{10}| \cdot e^{j\varphi_{2,h^{in}_{10}}} \cdot \left|S^c_{12,h_{50}\to h_{10}}\right| - |h^{in}_{20}| \cdot e^{j\varphi_{2,h^{in}_{20}}} \cdot \left|S^c_{12,h_{50}\to h_{20}}\right| + |h^{in}_{30}| \cdot e^{j\varphi_{2,h^{in}_{30}}} \cdot \left|S^c_{12,h_{50}\to h_{30}}\right| \\ |h^{in}_{10}| \cdot e^{j\varphi_{2,h^{in}_{10}}} \cdot \left|S^c_{12,h_{70}\to h_{10}}\right| + |h^{in}_{20}| \cdot e^{j\varphi_{2,h^{in}_{20}}} \cdot \left|S^c_{12,h_{70}\to h_{20}}\right| + |h^{in}_{30}| \cdot e^{j\varphi_{2,h^{in}_{30}}} \cdot \left|S^c_{12,h_{70}\to h_{30}}\right| \end{bmatrix} \tag{4}$$

As a next step, the phases of the excitation modes TE_{20} and TE_{30} are expressed as a function of the phase of the first excitation mode TE_{10} as:

$$\varphi_{2,h^{in}_{20}} = \varphi_{2,h^{in}_{10}} - \Delta\varphi^{in}_{20} \Rightarrow e^{j\varphi_{2,h^{in}_{20}}} = e^{j\varphi_{2,h^{in}_{10}}} \cdot e^{-j\Delta\varphi^{in}_{20}} \tag{5a}$$

$$\varphi_{2,h^{in}_{30}} = \varphi_{2,h^{in}_{10}} - \Delta\varphi^{in}_{30} \Rightarrow e^{j\varphi_{2,h^{in}_{30}}} = e^{j\varphi_{2,h^{in}_{10}}} \cdot e^{-j\Delta\varphi^{in}_{30}} \tag{5b}$$

Finally, we include the principle of energy conservation under the assumption that the output of the four excitation waveguides presents only the three afore-mentioned modes:

$$\sqrt{|h^{in}_{10}|^2 + |h^{in}_{20}|^2 + |h^{in}_{30}|^2} = 1 \Rightarrow |h^{in}_{10}| = \sqrt{1 - |h^{in}_{20}|^2 - |h^{in}_{30}|^2} \tag{6}$$

Therefore, by the inclusion of (5a)–(5b) and (6) into (4) and without loss of generality, after considering the phase of the mode h^{in}_{10}, $\varphi_{2,h^{in}_{10}}$ constant and equal to zero the last system of equations

takes the following form:

$$\begin{vmatrix} F_1^{h_{10}} \\ F_1^{h_{30}} \\ F_1^{h_{50}} \\ F_1^{h_{70}} \end{vmatrix} = 2 \begin{vmatrix} \sqrt{1-\left|h_{20}^{in}\right|^2-\left|h_{30}^{in}\right|^2}\cdot\left|S^c_{12,h_{10}\to h_{10}}\right|+\left|h_{20}^{in}\right|\cdot e^{-j\Delta\varphi_{20}^{in}}\cdot\left|S^c_{12,h_{10}\to h_{20}}\right|+\left|h_{30}^{in}\right|\cdot\left|S^c_{12,h_{10}\to h_{30}}\right|\cdot e^{-j\Delta\varphi_{30}^{in}} \\ \sqrt{1-\left|h_{20}^{in}\right|^2-\left|h_{30}^{in}\right|^2}\cdot\left|S^c_{12,h_{30}\to h_{10}}\right|-\left|h_{20}^{in}\right|\cdot e^{-j\Delta\varphi_{20}^{in}}\cdot\left|S^c_{12,h_{30}\to h_{20}}\right|-\left|h_{30}^{in}\right|\cdot\left|S^c_{12,h_{30}\to h_{30}}\right|\cdot e^{-j\Delta\varphi_{30}^{in}} \\ -\sqrt{1-\left|h_{20}^{in}\right|^2-\left|h_{30}^{in}\right|^2}\cdot\left|S^c_{12,h_{50}\to h_{10}}\right|-\left|h_{20}^{in}\right|\cdot e^{-j\Delta\varphi_{20}^{in}}\cdot\left|S^c_{12,h_{50}\to h_{20}}\right|+\left|h_{30}^{in}\right|\cdot\left|S^c_{12,h_{50}\to h_{30}}\right|\cdot e^{-j\Delta\varphi_{30}^{in}} \\ \sqrt{1-\left|h_{20}^{in}\right|^2-\left|h_{30}^{in}\right|^2}\cdot\left|S^c_{12,h_{70}\to h_{10}}\right|+\left|h_{20}^{in}\right|\cdot e^{-j\Delta\varphi_{20}^{in}}\cdot\left|S^c_{12,h_{70}\to h_{20}}\right|+\left|h_{30}^{in}\right|\cdot\left|S^c_{12,h_{70}\to h_{30}}\right|\cdot e^{-j\Delta\varphi_{30}^{in}} \end{vmatrix} \tag{7}$$

There are three points to be noted as far as Eq. (7) is concerned. The first one refers to the fact that the common waveguide modes TE_{10} and TE_{70} couple in the same way to the three excitation waveguide modes TE_{10}, TE_{20}, and TE_{30}. The next two comments regard the impact of the third excitation mode that has been considered in contrast to the previous moderate aperture size cases [9–11]; the TE_{30} mode ($|h_{30}^{in}|\cdot e^{-j\Delta\varphi_{30}^{in}}$). The interaction of this mode with the common waveguide mode $F_1^{h_{30}}$ [second line in Eq. (7)] acts similarly to the excitation mode TE_{20}. As a result, it couples 180° out of phase with the term $\sqrt{1-|h_{20}^{in}|^2-|h_{30}^{in}|^2}\cdot|S^c_{12,h_{30}\to h_{10}}|$ as the minus sign denotes. Likewise, for the case of the common mode $F_1^{h_{50}}$ [third line in Eq. (7)], the TE_{30} mode ($|h_{30}^{in}|\cdot e^{-j\Delta\varphi_{30}^{in}}$) couples 180° out of phase with both terms $\sqrt{1-|h_{20}^{in}|^2-|h_{30}^{in}|^2}\cdot|S^c_{12,h_{50}\to h_{10}}|$ and $|h_{20}^{in}|\cdot e^{-j\Delta\varphi_{20}^{in}}\cdot|S^c_{12,h_{50}\to h_{20}}|$ as the plus sign denotes. It is finally noted that the two first terms for the calculation of the common waveguide mode TE_{50} add in phase between one another and out of phase with the term $|h_{30}^{in}|\cdot|S^c_{12,h_{50}\to h_{30}}|\cdot e^{-j\Delta\varphi_{30}^{in}}$. However, the total phase of the common waveguide mode $F_1^{h_{50}}$ will be shifted by 180° (excluding the term $|h_{30}^{in}|\cdot|S^c_{12,h_{50}\to h_{30}}|\cdot e^{-j\Delta\varphi_{30}^{in}}$).

The vector on the left side of Eq. (7) represents the required modal distribution for the optimal approximation of a uniform electric field at the aperture, that is [3, 15]:

$$|F| = \begin{vmatrix} F_1^{h_{10}} \\ F_1^{h_{30}} \\ F_1^{h_{50}} \\ F_1^{h_{70}} \end{vmatrix} \approx \begin{vmatrix} 0.924 \\ 0.308 \\ 0.1848 \\ 0.132 \end{vmatrix} \tag{8}$$

Therefore, this is the scalar vector to which (7) is subject. Essentially, Eq. (7) is an overdetermined system with 4 equations and 2 complex unknowns; the terms $|h_{20}^{in}|\cdot e^{-j\Delta\varphi_{20}^{in}}$ and $|h_{30}^{in}|\cdot e^{-j\Delta\varphi_{30}^{in}}$. The solutions of these unknowns will define the design and optimization goals of the excitation waveguide section; the asymmetrically flared waveguide section to be designed.

2.2. Design and Results of the Excitation and the Common Waveguide Sections

The design and optimization of the excitation waveguide section as well as the upper (common) waveguide region of the total 4-port radiating element have been performed with MM by the commercially available software μWave Wizard [16].

Figure 4(a) illustrates the normalized voltage amplitude of the excitation modes and the reflection coefficient. The dominant mode h_{10}^{in} exhibits levels above 0.9. The h_{20}^{in} mode presents a flat level of

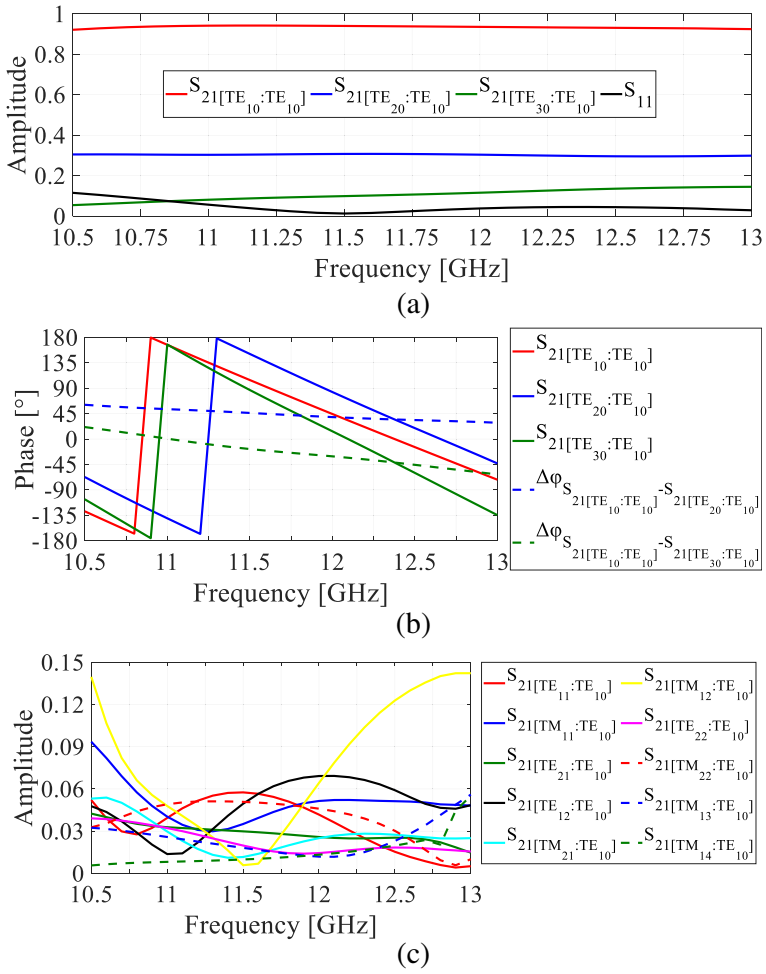

Figure 4. The optimized feeding waveguide section's results: (a) output amplitude of the modes TE_{10}, TE_{20} and TE_{30} and reflection coefficient at the input, (b) output phase of the modes TE_{10}, TE_{20} and TE_{30} and relative phase difference and (c) output amplitude of the rest higher order modes.

0.3, while the h_{30}^{in} mode varies between 0.08 and 0.14. The input reflection coefficient remains below 0.1 ($-20\,\text{dB}$). Fig. 4(b) depicts the absolute phase and relative phase difference of the three excitation modes. The values of $\Delta\varphi_{20}^{in}$ vary from 60° to 30° and of $\Delta\varphi_{30}^{in}$ from 15° to −55°. The amplitude of the rest undesired higher order modes presents values below 0.14 ($\approx -17\,\text{dB}$) as shown in Fig. 4(c). The total profile of the waveguide structure is around $2.6\lambda_0$.

Next, the common waveguide section was designed so that the phase content of the aperture modes canbe corrected. The guided wavelength is dependent on the cross-sectional dimensions of the square waveguide. The (upper) common waveguide part was designed with a slightly linearly flared waveguide section. From the common waveguide interface of the 4-furcation with dimensions $2 \cdot a_{10} + t = 96.9\,\text{mm}$, we end up to the final radiating aperture with dimensions a_{ap}. The total length of the common waveguide section is $L_{out} = 45.762\,\text{mm}$. This corresponds to $0.93\lambda_{g_{F_1^{h30}}}/\lambda_{g_{F_1^{h10}}} \approx 0.77\lambda_{g_{F_1^{h50}}}/\lambda_{g_{F_1^{h10}}} \approx 0.43\lambda_{g_{F_1^{h70}}}/\lambda_{g_{F_1^{h10}}}$ (where $\lambda_{g_{F_1^{hm0}}}$ the average guided wavelength) in order to maintain the required phase consistency of the modes F_1^{hm0} or TE_{m0}^{ap}, $m = 1, 3, 5, 7$. The flared waveguide section has been discretized into finite tapered waveguide parts with equal lengths; then the average guided wavelength has been computed for the calculation of the ratios.

3. COMPUTED RESULTS OF THE 4-PORT QFPH

The final tuning was performed with μWave Wizard [16], and last full-wave simulations in frequency (HFSS [17]) and time (CST [18]) domain verified the high aperture efficiency levels that the radiating element can attain.

Figure 5(a) illustrates the numerical results of the aperture modal amplitude and reflection coefficient at the input ports of the Q-FPH. The absolute phases as well as the relative phase difference of the aperture modes are illustrated in Fig. 5(b). For the calculation of the aperture modal content, the 4 orthomode ports have been excited simultaneously. Due to the transversal symmetry of the structure, the results are identical for both polarizations. The radiating element has been simulated as a 5-port network.

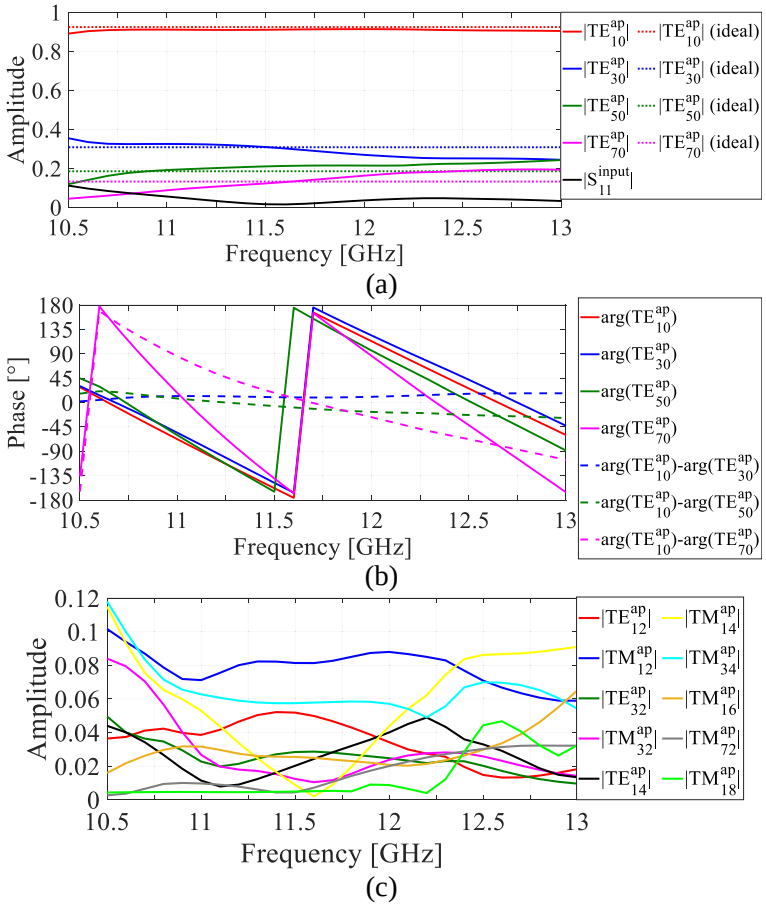

Figure 5. Modal results of the Q-FPH. (a) Amplitude of the aperture modes and input reflection coefficient, (b) phase of the aperture modes and relative phase difference and (c) amplitude of the rest higher order aperture modes.

Figure 5(a) shows that the designed Q-FPH excites the aperture modes with a very good agreement with respect to the ideal case. Besides, the phase difference between the aperture modes is low except for the TE_{70}, whose phase at the borders of the Ku-Tx frequency band is not consistent. This occurs due to the much larger guided wavelength (hence much lower propagation constant) in relation to the rest three aperture modes. The amplitude of the rest higher order modes exhibits levels below 0.09 (≈ -21 dB) as shown in Fig. 5(c).

Next, the Q-FPH was simulated in frequency (HFSS) and time (CST) domain using the same boundary conditions (Perfect Electric Conductor on the elements waveguide walls). Fig. 6 depicts the active reflection coefficient and mutual couplings among the 4 ports. The maximum cross-polarization,

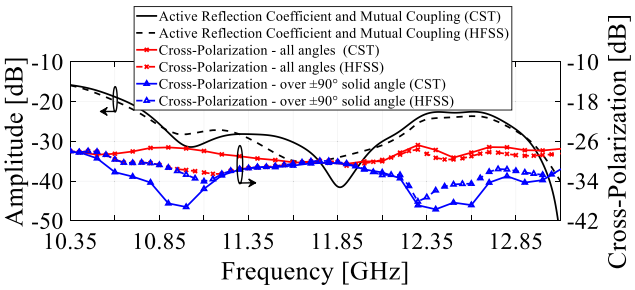

Figure 6. Simulated active S-parameters and max X-Pol of the Q-FPH.

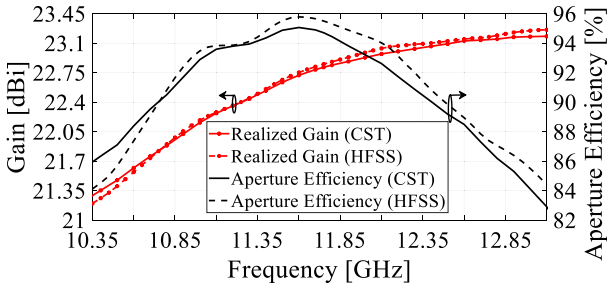

Figure 7. Simulated aperture efficiency and realized gain of the Q-FPH.

which is also illustrated, remains below −27 dB over all directions and below −30 dB for a solid angle of ±90°.

Figure 7 presents the simulated aperture efficiency and realized gain. A level above 90% over a fractional bandwidth of 14% (10.7 ∼ 12.4 GHz) is observed. The aperture efficiency can be further improved at the lower frequencies for a better reflection coefficient level which is responsible for the decrease of the realized gain. The level of reflection coefficient can be improved after the optimized inclusion of the excitation network [19]. The discrepancies between the two electromagnetic solvers lie below ±0.1 dB in terms of simulated realized gain. This is translated to an aperture efficiency difference of less than ±1.5%. These discrepancies are attributed to the different solving methods and the level of uncertainty induced by the meshing of each method.

Figure 8(a) depicts the simulation result with CST distribution of the electric field amplitude at the central frequency of 11.7 GHz on the aperture plane of the 4-port radiating element. Likewise, Fig. 8(b) depicts the distribution of the electric field phase. The radiating element is polarized along x-axis in both figures. As expected by the calculated aperture modes, the electric field is distributed in a uniform way.

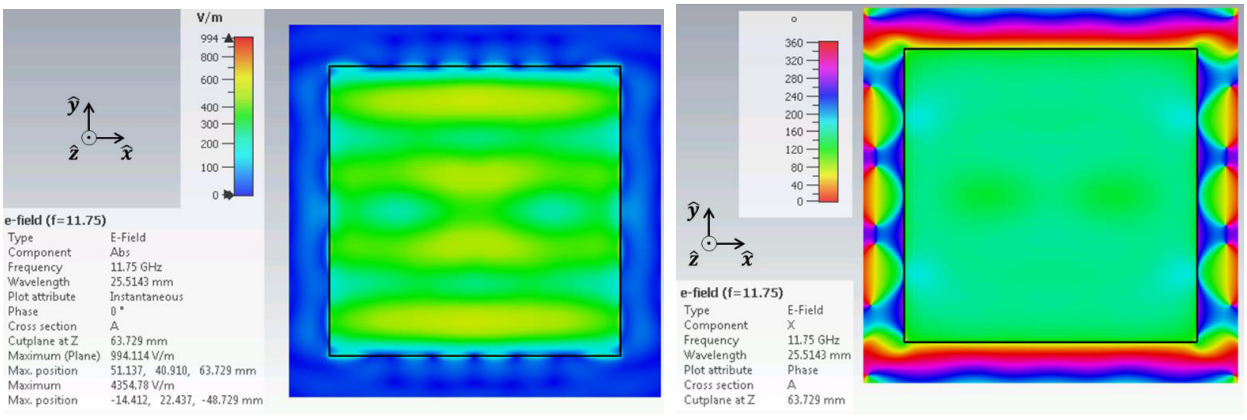

(a) (b)

Figure 8. Simulated electric field distribution at the central frequency of 11.7 GHz on the aperture plane of the 4-port radiating element. (a) Amplitude. (b) Phase.

Figures 9(a)–(d) show the simulated normalized far-field directivity pattern at 11.7 GHz (circled lines). The co-polarized pattern is shown for the three principal cuts [$\varphi = 0°$, 45°, 90° in Figs. 9(a)–(c), respectively] and the cross-polarized pattern at the D-plane [$\varphi = 45°$ in Fig. 9(d)]. In the same figures, the ideal case is superimposed (solid lines). This is the case of an aperture with the same dimensions illuminated by a uniform and unidirectional electric field. After applying the equivalence principle, we obtain the directivity patterns of this identical with our case aperture which produces the maximum

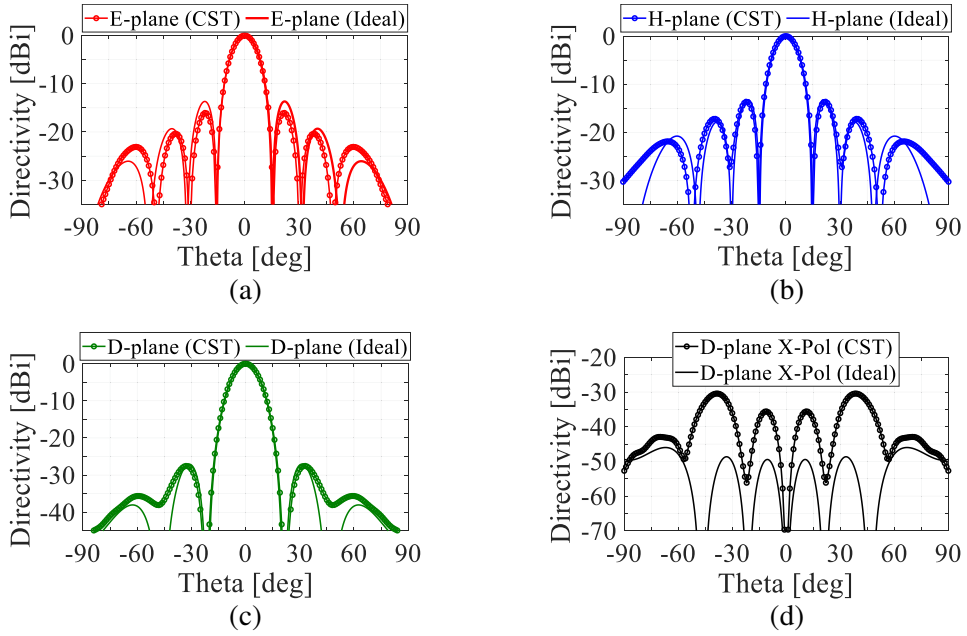

Figure 9. Normalized radiation pattern cuts ($f_0 = 11.7\,\text{GHz}$): (a) co-polar e-plane, (b) co-polar h-plane, (c) co-polar d-plane, (d) cross-polar (X-Pol) d-plane. Solid line: ideal. Circled line: simulated results.

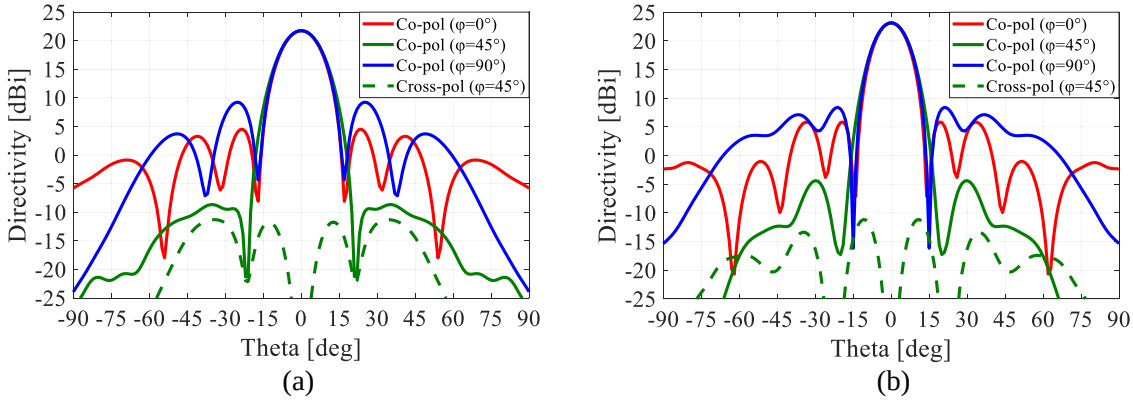

Figure 10. Simulated radiation patterns of the 4-port radiating element: (a) 10.7 GHz and (b) 12.7 GHz.

directivity radiation pattern (i.e., 100% aperture efficiency). A very close agreement between the two cases is observed, displaying the excellent radiation performance of the Q-FPH.

Figure 10 depicts the simulated normalized directivity patterns (the co-polar in the three principal plane cuts and the cross-polar in D-plane) of the 4-port radiating element at 10.7 GHz and 12.7 GHz. These patterns are characterized by rotational symmetry as well. The cross-polarization level is below $-30\,\text{dB}$ for a solid angle of $\theta \leq \pm 90^\circ$ and below $-32\,\text{dB}$ for a solid angle of $\theta \leq \pm 15^\circ$. At $f_{\text{high}} = 12.7\,\text{GHz}$, the H-plane co-polar component presents increased radiation level outside the main lobe. This is attributed to the amplitude and phase differentiation between the aperture modes referring to the modal solutions in Fig. 5. In particular, the relative phase difference of the TE_{70} aperture mode with respect to the rest aperture modes (TE_{10}, TE_{30} and TE_{50}) gets values above 70° after 12.5 GHz. Besides, its amplitude increases above the level of 0.2, while the optimum is around 0.15.

The radiating element's axial profile length is 127.46 mm ($4.97\lambda_0$). It achieves aperture efficiency above 90% for a wide frequency bandwidth (over 14%); it is noted that the maximum theoretical level has been calculated 95.1% [15].

Table 1. State-of-the-art square aperture and high efficiency horns.

Ref. →	[3]	[4]	[5]	This work
Aperture Size	$4\lambda_0 \times 4\lambda_0$	$4\lambda_0 \times 4\lambda_0$	$4\lambda_0 \times 4\lambda_0$	$4\lambda_0 \times 4\lambda_0$
Bandwidth (%)	12	2.5	20	20
Aperture Efficiency (%)	85–88	85	84–90.5	86–95
Min Return Loss (dB)	25	N/A	23.5	20
Max Cross-Pol (dB)	−25	N/A	−21.5	−27
Profile (λ_0)	9.56	4.4	11.75	4.53
Horn Antenna Type	Profiled	Subarray	Profiled	Q-FPH

Table 1 includes the radiating elements that provide the better aperture efficiency than the Q-FPH optimized by the presented generalized methodology. Fig. 11 depicts a more detailed view of the aperture efficiency across the normalized frequency bandwidth between the horn in [5] and the Q-FPH. The element in [5] delivers the best aperture efficiency × bandwidth product among all solutions in the literature. The design case of the $4\lambda_0 \times 4\lambda_0$ Q-FPH conceived to describe and verify the presented methodology achieves an average aperture efficiency augmentation of 3.5% over a 20% relative bandwidth and a profile reduction of $7.2\lambda_0$ with respect to the state-of-the-art profiled horn from [5].

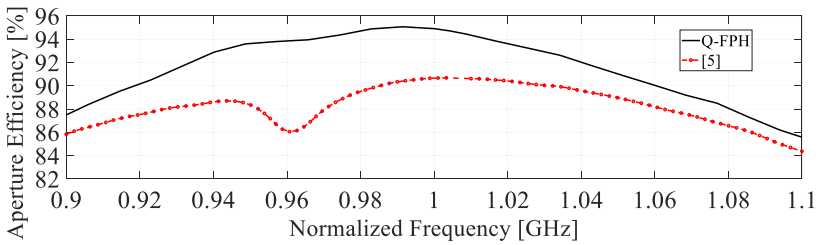

Figure 11. Aperture efficiency vs frequency of the Q-FPH and the profiled horn from [5] selected as that radiating element with a $4\lambda_0 \times 4\lambda_0$ aperture that achieves the best aperture efficiency × bandwidth product.

Experimental verification of structurally similar high aperture efficiency Bi- and Quad-FPH elements can be found in [10] and [11], respectively. These antennas have electrically moderate square aperture sizes and were developed before the generalization of the methodology presented in this paper. It is last mentioned that although the presented design case has been characterized numerically without including materials and hence loss analysis, from former knowledge [11], ohmic losses of about 0.1 dB are expected for non-treated 3D-metal printed antenna feeds which employ the 4-port radiating element with the feeder [19].

4. CONCLUSION

We present here the extended methodology for the design of Q-FPHs. We extract the 4-furcation's GSM and provide analytical expressions for the calculation of the appropriate excitation of the four feeding waveguide sections. Based on this analysis, the design is reducesd to the optimization of one (out of the four) feeding and the upper waveguide sections with the rigorous mode-matching method. The numerically calculated results of a design case of a $4\lambda_0 \times 4\lambda_0$ Q-FPH prove the extensibility and robustness of the method.

REFERENCES

1. Shafai, L., S. K. Sharma, and S. Rao, *Handbook of Reflector Antennas and Feed Systems: Feed Systems*, Vol. 2, Artech House Antennas and Propagation Library, Artech House, Norwood, MA, USA, 2013.
2. Chan, K. K. and S. K. Rao, "Design of high efficiency circular horn feeds for multibeam reflector applications," *IEEE Trans. Antennas Propag.*, Vol. 56, No. 1, 253–258, Jan. 2008.
3. Bhattacharyya, A. K. and G. Goyette, "A novel horn radiator with high aperture efficiency and low cross-polarization and applications in arrays and multibeam reflector antennas," *IEEE Trans. Antennas Propag.*, Vol. 52, No. 11, 2850–2859, Nov. 2004.
4. Catalani, A., L. Russo, O. M. Bucci, T. Isernia, A. F. Morabito, S. Perna, D. Pinchera, and G. Toso, "Sparse arrays for satellite communications: From optimal design to realization," *32nd ESA Antenna Workshop*, Noordwijk, The Netherlands, Oct. 5–10, 2010.
5. Agastra, E., G. Bellaveglia, L. Lucci, R. Nesti, G. Pelosi, G. Ruggerini, and S. Selleri, "Genetic algorithm optimization of high-efficiency wide-band multimodal square horns for discrete lenses," *Progress In Electromagnetics Research*, Vol. 83, 335–352, 2008.
6. Sotoudeh, O., P.-S. Kildal, P. Ingvarson, and S. P. Skobelev, "Single- and dual-band multimode hard horn antennas with partly corrugated walls," *IEEE Trans. Antennas Propag.*, Vol. 54, No. 2, 330–339, Feb. 2006.
7. Lier, E., D. H. Werner, and T. S. Bird, "The evolution from metal horns to metahorns: The development of EM horns from their inception to the present day," *IEEE Antennas Propag. Mag.*, Vol. 61, No. 4, 6–18, Aug. 2019.
8. Fraysse, J.-P., C. Stoumpos, H. Legay, and S. Tubau, "Multiple-port radiating element," US Patent, Pub. No. US 2020/0176878 A1, Jun. 4, 2020.
9. Stoumpos, C., J.-P. Fraysse, G. Goussetis, R. Sauleau, C. G. González, and H. Legay, "Compact and highly efficient single and dual polarized aperture antennas with integrated multiport overmoded excitation," *Proc. 15th Eur. Conf. Antennas Propag. (EuCAP'21)*, 1–5, Mar. 2021.
10. Stoumpos, C., J.-P. Fraysse, G. Goussetis, C. G. González, R. Sauleau, and H. Legay, "Highly efficient broadband pyramidal horn with integrated H-plane power division," *IEEE Trans. Antennas Propag.*, Vol. 70, No. 2, 1499–1504, Feb. 2022.
11. Stoumpos, C., J.-P. Fraysse, G. Goussetis, R. Sauleau, and H. Legay, "Quad-furcated profiled horn: The next generation highly efficient GEO antenna in additive manufacturing," *IEEE Open J. Antennas Propag.*, Vol. 3, 69–82, 2022.
12. Rao, S. K. and C. Ostroot, "Design principles and guidelines for phased array and reflector antennas," *IEEE Antennas Propag. Mag.*, Vol. 62, No. 2, 74–81, Apr. 2020.
13. Angeletti, P., G. Toso, and G. Ruggerini, "Array antennas with jointly optimized elements positions and dimensions. Part II: Planar circular arrays," *IEEE Trans. Antennas Propag.*, Vol. 62, No. 4, 1627–1639, Apr. 2014.
14. Nadarassin, M., et al., "PAFSR reconfigurable antenna feed array design," *Proc. 15th Int. Symp. Antenna Technol. Appl. Electromagn.*, 1–6, Jun. 2012.
15. Polo-López, L., J. Córcoles, J. A. Ruiz-Cruz, J. R. Montejo-Garai, and J. M. Rebollar, "On the theoretical maximum directivity of a radiating aperture from modal field expansions," *IEEE Trans. Antennas Propag.*, Vol. 67, No. 4, 2781–2786, Apr. 2019.
16. Mician μWave Wizard, MICIAN GmbH. [Online]. Available: www.mician.com.
17. ANSYS HFSS, 3D Full-wave Electromagnetic Field Simulation by Ansoft. [Online]. Available: www.ansys.com.
18. Computer Simulation Technology (CST). Accessed on: January 12, 2021. [Online]. Available: www.3ds.com.
19. Stoumpos, C., J.-P. Fraysse, G. Goussetis, R. Sauleau, C. G. González, T. Pierré, and H. Legay, "Four-way orthomode waveguide power dividers: Subtractive and additive manufacturing," *Proc. 15th Eur. Conf. Antennas Propag. (EuCAP'21)*, 1–5, Mar. 2021.